

# Antimicrobial and Pro-Osteogenic Coaxially Electrospun Magnesium Oxide Nanoparticles-Polycaprolactone /Parathyroid Hormone-Polycaprolactone Composite Barrier Membrane for Guided Bone Regeneration

Yiwen Dong<sup>1,3</sup>, Litao Yao<sup>2-4,\*</sup>, Lei Cai<sup>1</sup>, Mi Jin<sup>1</sup>, Tymour Forouzanfar<sup>2,3</sup>, Lianjun Wu<sup>1</sup>, Jinsong Liu<sup>1,\*</sup>, Gang Wu<sup>2,3</sup>

<sup>1</sup>School and Hospital of Stomatology, Wenzhou Medical University, Wenzhou, People's Republic of China; <sup>2</sup>Department of Oral and Maxillofacial Surgery/Pathology, Amsterdam UMC and Academic Center for Dentistry Amsterdam (ACTA), Vrije Universiteit Amsterdam, Amsterdam Movement Science, Amsterdam, the Netherlands; <sup>3</sup>Department of Oral Cell Biology, Academic Centre for Dentistry Amsterdam (ACTA), University of Amsterdam (UvA) and Vrije Universiteit Amsterdam (VU), Amsterdam, the Netherlands; <sup>4</sup>Department of Dentistry, Sir Run Run Shaw Hospital, School of Medicine, Zhejiang University, Hangzhou, Zhejiang, People's Republic of China

\*These authors contributed equally to this work

Correspondence: Litao Yao, Department of Dentistry, Sir Run Run Shaw Hospital, School of Medicine, Zhejiang University, Hangzhou, People's Republic of China, Zhejiang, Email yaolt@srrsh.com; Jinsong Liu, School and Hospital of Stomatology, Wenzhou Medical University, Wenzhou, 325027, People's Republic of China, Email jinsong0719@wmu.edu.cn

**Introduction:** An antibacterial and pro-osteogenic coaxially electrospun nanofiber guided bone regeneration (GBR) membrane was fabricated to satisfy the complicated and phased requirements of GBR process.

**Methods:** In this study, we synthesize dual-functional coaxially electrospun nanofiber GBR membranes by encapsulating parathyroid hormone (PTH) in the core layer and magnesium oxide nanoparticles (MgONPs) in the shell layer (MgONPs-PCL/PTH-PCL). Herein, the physicochemical characterization of MgONPs-PCL/PTH-PCL, the release rates of MgONPs and PTH, and antibacterial efficiency of the new membrane were evaluated. Furthermore, the pro-osteogenicity of the membranes was assessed both in-vitro and in-vivo.

**Results:** We successfully fabricated a coaxially electrospun nanofiber MgONPs-PCL/PTH-PCL membrane with the majority of nanofibers (>65%) ranged from 0.40~0.60µm in diameter. MgONPs-PCL/PTH-PCL showed outstanding antibacterial potential against *Escherichia coli* (E. coli) and *Staphylococcus aureus* (S. aureus) through the release of MgONPs. We also discovered that the incorporation of MgONPs significantly prolonged the release of PTH. Furthermore, both the in-vivo and in-vitro studies demonstrated that high dosage of PTH promoted pro-osteogenicity of the membrane to improve bone regeneration efficacy with the presence of MgONPs.

**Conclusion:** The new composite membrane is a promising approach to enhance bone regeneration in periodontitis or peri-implantitis patients with large-volume bone defects.

**Keywords:** antibacterial property, pro-osteogenicity, coaxially electrospun, barrier membrane, guided bone regeneration

## Introduction

Guided bone regeneration (GBR) technique is the most widely used surgical procedure that adopts barrier membranes and particulate bone-defect-filling materials to restore bone volume and dimensions surrounding natural teeth or artificial implants.<sup>1</sup> In the classic GBR concept, barrier membranes mainly function to prevent the invasion of surrounding connective tissues to provide a favorable microenvironment to facilitate osteoblast proliferation, migration, differentiation and finally bone tissue regeneration.<sup>1</sup> However, the efficacy of GBR may be greatly challenged by many adverse conditions, such as

inflammation and large-volume bone defects that are resulted from severe periodontitis or peri-implantitis.<sup>2,3</sup> On one hand, large-volume bone defects may largely surpass the spontaneous healing ability of bone tissue and will be healed only by connective tissues. One approach to this problem is the adoption of autologous bone chips, whose use is, whereas, associated with limited availability, donor site pain and morbidity.<sup>4</sup> Furthermore, periodontitis or peri-implantitis-derived inflammation may further compromise the healing capacity of bone tissue.<sup>5,6</sup> On the other hand, residual bacteria that escape from the chemical and mechanical elimination procedures may rapidly proliferate and form biofilms, resulting in a series of complications, such as post-operative infection, bone graft exposure and impeded bone regeneration.<sup>7</sup> In clinic, systemic administration of antibiotics is conventionally applied to combat these complications. However, its application is also associated with certain concerns, such as dysbacteriosis, poor biodistribution, toxicity and bacterial resistance.<sup>8,9</sup> In recent years, multi-functionalized biomaterials used for GBR membranes with antibacterial and pro-osteogenic properties have shown promising application potential to cope with these complicated adverse conditions.

One of the commonly used approaches to synthesize a multi-functionalized membrane is coaxial electrospinning which involves the arrangement of multiple solution feed systems to simultaneously electrospun two or more polymer solutions to form core-shell structured nanofibers. This technique allows for the encapsulation of two different bioactive agents respectively into core and shell layers, enabling their sustained releases.<sup>10</sup>

Due to the complexity of the oral flora, broad-spectrum antibiotics are frequently applied in membrane in previous studies.<sup>11</sup> However, compared with clinically available antibiotics, antibacterial metallic nanoparticles are a promising alternative due to their significantly broader antimicrobial spectrum while lowering the risk of bacterial resistance.<sup>10,12</sup> Silver-based nanoparticles, a frequently used antibacterial metallic nanoparticle, are associated with several concerns, such as local accumulation of heavy metal elements causing cytotoxicity.<sup>13</sup> In contrast, magnesium oxide nanoparticles (MgONPs) possess biodegradability and lower toxicity.<sup>14</sup> Furthermore, the benefits of MgONPs, which includes pro-osteogenic property<sup>15</sup> and significant inhibition of biofilm formation and maturation, have attracted increasing interest in membrane applications.<sup>14</sup> As for the pro-osteogenic drug applied in GBR membrane, PTH is a suitable candidate. As a commonly used drug for bone regeneration, PTH promotes osteogenesis by activating osteoblast cells and the secretion of SOST through the receptor PTHr1.<sup>16,17</sup> Additionally, the cost of PTH is much lower than that of bone morphogenetic proteins, making it more readily available for clinical applications. At the same time, previous studies have proven that locally delivered PTH significantly promotes bone regeneration.<sup>16,18</sup> Moreover, Dang et al also demonstrated the synergistic effects of Mg and PTH in promoting bone regeneration.<sup>18</sup> Polycaprolactone (PCL) has been widely used as the scaffold in bone regeneration engineering,<sup>19,20</sup> therefore, we applied PCL in the nanofiber as the main scaffold.

In this study, we aimed to synthesize dual-functional coaxially electrospun nanofiber GBR membranes to achieve a sustained release by encapsulating PTH in the core layer and MgONPs in the shell layer (MgONPs-PCL/PTH-PCL). Herein, the physicochemical characterization of MgONPs-PCL/PTH-PCL, the release rates of MgONPs and PTH, and antibacterial efficiency of the new membrane were evaluated. Furthermore, the pro-osteogenicity of the membranes was assessed both in-vitro and in-vivo. The scheme of preparation and functional assessments of MgONPs-PCL/PTH-PCL coaxially electrospun barrier membrane is listed in [Figure 1](#).

## Materials and Methods

### PCL and MgONPs-PCL/PTH-PCL Coaxial Electrospinning Barrier Membrane

#### Preparation

In the coaxial electrospinning process, two needles of different gauge diameters were used. The diameter of the needle for core layer was 0.33mm and for shell layer was 1.10mm. The two needles were arranged in a concentric manner to dispense two separate solutions at the same time. The base solution was made up of polycaprolactone (PCL, Mn 70,000–90,000) and 2,2,2-Trifluoroethanol (TFE, purity > 99.0) with a concentration of PCL at 150mg/mL. The core solution was made by combining the base solution with different concentrations of PTH; the shell solution was made by mixing the base solution with or without MgONPs (nano-powder, diameter <50nm, PCL: MgONPs = 1:0.3). The concentration of MgONPs was altered by the pre-experiment results of SEM ([Supplement Data Figure S1](#)) and antibacterial assay ([Supplement Data Figure S2](#)). All the drugs were purchased from Sigma Aldrich. The voltage was 17kV and the distance

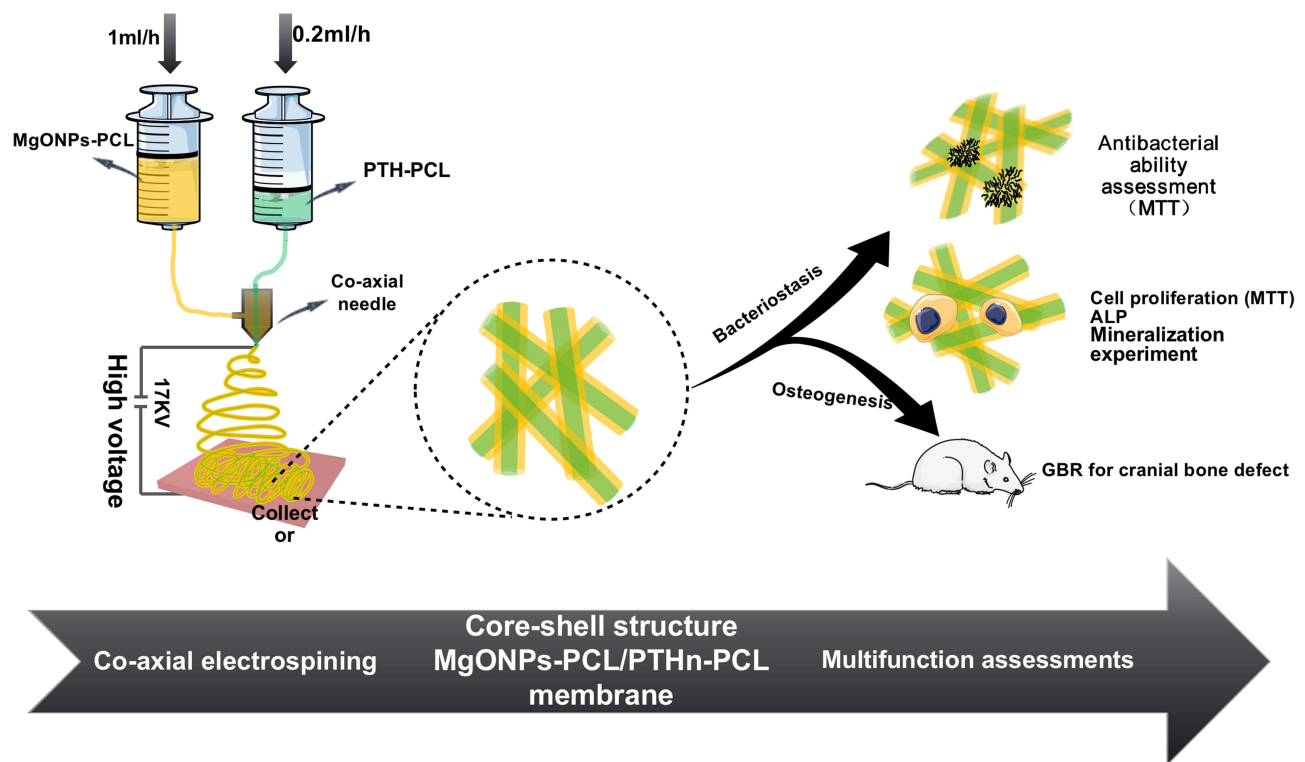


**Figure 1** Scheme of preparation and functional assessments of MgONPs-PCL/PTHn-PCL coaxially-electrospun barrier membrane.

between the top of the needles and the receptor was 10cm. The feed rate for the core was 0.2mL/h and for the shell it was 1mL/h. The procedure was kept at room temperature for 7h. The results of a scanning electron microscope (SEM) (Nova NanoSEM200, FEI Co., USA) and an antibacterial test were used to determine the optimum concentrations for base solution and MgONPs. The PCL membrane was fabricated with only the base solution in the same electrospinning parameter of MgONPs-PCL/PTHn-PCL (n represented the different concentrations of PTH). The MgONPs-PCL/PTHn-PCL membrane was labeled as group B and the PCL membrane was labeled as group A.

## Sample Characterization

The surface morphology and surface elemental composition of PCL and MgONPs-PCL/PTHn-PCL membrane were assessed by Field-emission scanning electron microscopy (Nova NanoSEM200, FEI Co., Houston, TX, USA) coupled with Energy dispersive X-ray (EDX) spectroscopy. The pore size and nanofiber diameter distribution of each membrane were estimated by the software Image J (National Institutes of Health, Bethesda, MD, USA) from the SEM micrographs. For calculating the pore size, the threshold function was applied to separate the pore area from the whole image. Subsequently, the analyzed particle function was used to calculate individual pores. The quantitative analysis of EDX was selected randomly from the SEM results and repeated three times. The chemical groups of the materials were evaluated by FTIR (Equinox 55, Bruker Co., Germany). The XRD (D8 Focus, Bruker Co.) with operating settings of 35 kV and 30mA was used to assess the crystalline phase in PCL and MgONPs-PCL/PTHn-PCL membranes. The data were collected at a scanning rate of 0.06°/s in the 2θ range of 10°~80°.

## In-vitro Evaluation of MgONP and PTH Release Kinetics

To test the release profiles of MgONPs in-vitro, group A and B (0.5 \* 1.5 \* 1.5cm) were immersed individually in 10mL of phosphate buffered solution (PBS) at 37°C and agitated at 100rpm. At 1, 3, 5, 7, 9, 11, 13, 15, 17, 19, 21, 23, 25, 27, and 29d, samples were removed from the solution and rinsed three times with fresh PBS before soaking in fresh buffer solutions of the same volume. Afterwards the solutions were mixed with aqua regia solution in a 1:1 vol ratio to dissolve

the MgONPs. The inductively coupled plasma-atomic emission spectroscopy (ICP-AES, OPTIMA8000, PerkinElmer, USA) was used to examine the magnesium ion concentration of solutions. The accumulative magnesium ion concentration was calculated using the formula:

$$c = (c_1 - c_0) + (c_2 - c_0) + (c_3 - c_0) + \dots + (c_n - c_0)$$

$c$  refers to the accumulative magnesium ion concentration;  $c_1$  refers to the magnesium ion concentration of the solution at day 1;  $c_2$  refers to the magnesium ion concentration of the solution at day 3 and so on;  $c_0$  refers to the magnesium ion concentration of the fresh PBS solution.

The MgONPs released from the MgONPs-PCL/PTHn-PCL coaxial electrospinning barrier membrane were exactly proportional to the accumulative magnesium ion concentration. PTH was substituted by the model protein bovine serum albumin, which had been conjugated with fluorescein isothiocyanate (BSA-FITC, sigma), marked as group C (PCL/BSA-FITC-PCL) and group D (MgONPs-PCL/BSA-FITC-PCL). To evaluate the release kinetics of PTH from the membrane, 6 $\mu$ g of BSA-FITC was added to the core of the nanofibers of the membrane. The samples of group C and group D were immersed in 10mL PBS solution, respectively. Subsequently, the process of group A and group B samples was repeated for Group C and D. According to the methodology reported previously, the spectrophotometer was used to examine the sampled solutions of groups C and D.<sup>21</sup> In each group, three replicates were set.

## Antibacterial Efficacy of PCL and MgONPs-PCL/PTH-PCL Coaxial Electrospinning Barrier

All the samples used in antibacterial ability tests, cell experiments, and animal experiments were sterilized by submerging them in a 75% ethyl alcohol solution for 1h and then drying before use. The entire procedure was carried out on a clean bench with laminar flow.

*S.aureus* (gram-positive bacteria) and *E.coli* (gram-negative bacteria) were used to test the antibacterial efficacy of PCL and MgONPs-PCL/PTH-PCL. The method was used in our earlier study with modification.<sup>22</sup> Briefly, samples ( $\phi=14$ mm) were separated into groups, co-cultured with 500 $\mu$ L *S.aureus* (ATCC 25923) or *E.coli* (ATCC 25922) ( $1 \times 10^6$ CFU/mL) buffer solution and 500 $\mu$ L Luria-Bertani culture and agitated at 100rpm at 37°C for 24h. After that, the samples were removed and rinsed three times with fresh PBS.

About 200 $\mu$ L of each co-culture solution was put into a 1.5mL centrifuge tube, along with 20 $\mu$ L of MTT (0.5mg/mL, Aladdin, Shanghai, China) stock solution, manually mixed for 10s, and incubated for 20min at 37°C. The mixture was centrifuged, and the supernatant was removed. Using a pipette, added 150 $\mu$ L DMSO (AR, Aladdin, Shanghai, China) into the pellets of the cell-formazan crystal complex. Afterwards, we transferred the mixtures to 96-well plates and used a microplate reader (Bio-Rad Model 680, US) to detect absorbance at 540nm.<sup>23</sup> DMSO was applied as a control. In each group, three replicates were set.

## Effect of PCL and MgONPs-PCL/PTH-PCL Coaxial Electrospinning Barrier Membrane on Osteoblast Proliferation, Differentiation and Mineralization

The pure PCL membrane and MgONPs-PCL/PTH-PCL membranes ( $\phi=14$ mm) with varied concentrations of PTH were separated into distinct groups and indicated in cell tests. According to the results of the pre-experiment, we screened out two concentrations (20 $\mu$ g/mL and 40 $\mu$ g/mL) of PTH with significant differences in cell experiments ([Supplement Data Figure S3](#)); labeled them as MgONPs-PCL/PTH20-PCL and MgONPs-PCL/PTH40-PCL, respectively. It was divided into four groups: A (MgONPs-PCL/PTH20-PCL), B (MgONPs-PCL/PTH40-PCL), C (MgONPs-PCL/PCL), and D (PCL). The mouse embryonic precursor osteoblast cells (MC3T3-E1 cells, ATCC, Chinese Academy of science, Shanghai, China) were cultured in alpha-minimum essential medium ( $\alpha$ -MEM). Ten percent fetal bovine serum (FBS) (Gibco, Invitrogen, Grand Island, NY, USA), 10 $\mu$ g/mL penicillin, 10 $\mu$ g/mL streptomycin, and 50 $\mu$ g/mL fungizone (complete medium) were added into the medium and cultured under the condition of 5%CO<sub>2</sub>, at 37°C. Medium was changed every 3d. Until the cell confluence reached about 80%–90%, cell passage was carried out. 0.25% trypsin and

0.1% EDTA were used for harvesting osteoblasts. Cells were then seeded onto 4 groups of membranes at  $2 \times 10^4$  cells/well, respectively and cultured in a Petri dish with complete medium.

### Cell Proliferation Assay

The proliferation of MC3T3-E1 seeded on the different membranes was detected using Cell Counting Kit-8 reagent (CCK-8, Beyotime Biotechnology, Shanghai, China) by measuring absorbance after incubation for 4 and 7d. MC3T3-E1 cells were seeded on different groups of membranes at a density of  $2 \times 10^4$  cells/well in the 24-well culture plates. After culturing for 4 and 7d, the medium was removed, cells were rinsed with PBS and incubated with 10% CCK-8 for 2h at 37°C in the dark. Afterwards, 100 $\mu$ L solution of each well were taken out and added to the 96-well culture plates. The absorbance value was determined at an optical density of 490nm using a Bio Rad microplate reader (Bio-Rad 680, USA). Four replicates were set in each group.

### Alkaline Phosphatase (ALP) Activity Characterization

MC3T3-E1 cells were seeded on different groups in  $\alpha$ -MEM at a concentration of  $2 \times 10^4$  cells/well. After incubation for 24h in the 24-well culture plates, the  $\alpha$ -MEM was replaced by mineralized induction medium (supplemented with 10mmol/l  $\beta$ -glycerophosphat, 0.05mmol/l acetic acid, and 100mmol/l dexamethasone) and it was changed every 3d in the following process. The membranes and cells were cultured in the mineralized induction medium for 7d. MC3T3-E1 cells on different membranes were lysed by 1% Triton X-100 at 0°C for 30min. Then, the lysates were measured via LabAssay™ ALP colorimetric assay kit (Wako Pure Chemicals, Japan), and the total intracellular protein content was tested by BCA Protein Assay Kit (Beyotime, China). In each group, four replicates were set.

### Mineralization Measurement

For the measurement of calcium deposits, MC3T3-E1 cells were seeded on different groups of membranes and cultured with the mineralized induction medium (four replicates per group) for 14d. The medium culture was freshly changed every 3d. After 14d of culture on four groups of membranes, MC3T3-E1 cells were rinsed with fresh cold PBS and fixed using 4% paraformaldehyde solution for 30min. Subsequently, extracellular matrix mineralization was evaluated by alizarin red staining (ARS, Solarbio, China). The dyed calcium nodules were finally dissolved in 10wt% cetylpyridinium chloride solution and measured by a Bio Rad microplate reader at OD540nm.

## The Assessment of Bone Reconstruction Promoting Effect of PCL, MgONPs-PCL/PCL and MgONPs-PCL/PTH-PCL Coaxial Electrospinning Membrane in-vivo Animals

In a pathogen-free environment, sixteen male Sprague-Dawley rats (Animal Centre, Wenzhou Medical University, 200–300g) were housed in pairs. The rats were acclimated to a regular rat chow diet, tap water, and a controlled temperature (25°C, relative humidity of 45–62%, and a 12h light-dark cycle). Animals were cared in accordance with the ethical guidelines of the Wenzhou Medical University Animal Care and Use Committee. The Animal Experimental Ethical Panel, Wenzhou Medical University, accepted the study protocol (Approval number: wydw2019-0658).

### Implantation Procedure

After a week of acclimation, 16 rats were placed into four groups randomly. Briefly, the rats were anesthetized by intraperitoneal injections of 10% chloral hydrate (3.3mL/kg). All the defects were 8 mm in diameter and were smooth punched with burs. As previously described,<sup>24</sup> critical size defects were created in calvaria, membranes were cut to the same size ( $\phi=10$ mm), and *S. aureus* ( $1 \times 10^6$ CFU/mL, 10 $\mu$ L) was mixed with deproteinized bovine bone mineral (DBBM, Geistlich Trading (Beijing) Co. Ltd, China, 0.2g) and divided into four groups: A.PCL + DBBM + *S. aureus*, B.MgONPs-PCL/PCL + DBBM + *S. aureus*, C. MgONPs-PCL/PTH20-PCL + DBBM + *S. aureus* and D.MgONPs-PCL/PTH40-PCL+DBBM+S. aureus. We implanted the four different groups of grafts into the defects separately and closed the wound with tight suture. A month after implantation, the rats were sacrificed and the calvaria bone was harvested. The calvarial specimens were fixed in 4% paraformaldehyde (Yili FineChemical Co., Ltd, China) for 48h. Micro-CT and histological analysis were used to assess the samples.

## Micro-CT Analysis

A micro-CT scanner ( $\mu$ CT100, SCANCO Medical AG, Switzerland) was used to monitor the samples for new bone regeneration in the defect areas. For qualitative and quantitative evaluation, about 300 binary images were rebuilt into three-dimensional images. The bone volume/total bone ratio (BV/TV), trabecular thickness (Tb.Th), trabecular number (Tb.N), and trabecular separation (Tb.Sp) were calculated to detect the quality and quantity of new bone in different groups.

## Histology Sample Preparation

After micro-CT scanning, 10% EDTA solution was applied for the demineralization of calvarial specimens, and the solution was replaced every day for 3 months. The samples were grade dehydration using an ethanol series, which further replaced by a xylene, and routinely embedded in paraffin. A sliding microtome (EXAKT300CP, Germany) was used to cut the specimens. The thickness of paraffin sections was set to 5 $\mu$ m. Hematoxylin and Eosin (H&E) staining was used on the central sections of each defect. The Leica DMI4000B microscope was used to examine them in sagittal perspectives. Quantity analysis of the samples (new bone surface/graft materials surface) were analyzed by Image J.

## Statistical Analysis

The results were reported as the mean  $\pm$  standard deviation. Statistical analysis was performed by Student's *t*-test and one-way analysis of variance (ANOVA). Difference at  $p < 0.05$  was considered to be significant.

## Results and Discussion

### Physicochemical Characterization

#### SEM and EDX Observation

The representative SEM morphology of pure PCL and MgONPs-PCL/PTH-PCL composite membranes are depicted in Figure 2A1 and A2, respectively. The surface morphology of both membranes was composed of randomly oriented fibers without bead-like structure, indicating the successful fabrication of the electrospun nanofibers. The fibers in pure PCL (Figure 2A1) were smooth, while those in the composite membrane (Figure 2A2) exhibited some lumps, which may be due to the occasional aggregation of MgONPs.<sup>25,26</sup> The diameter size distribution of nanofibers in each membrane was measured from the micrographs and listed in Figure 2B1 and B2, respectively. The fiber diameter of pure PCL was at a range of 0.22~2.06 $\mu$ m and that of MgONPs-incorporated membrane was 0.33~1.51 $\mu$ m. The majority of nanofibers (>65%) that ranged from 0.40~0.60 $\mu$ m in diameter, has been proved by Chen et al to be more optimal in promoting cell adhesion and proliferation.<sup>27</sup>

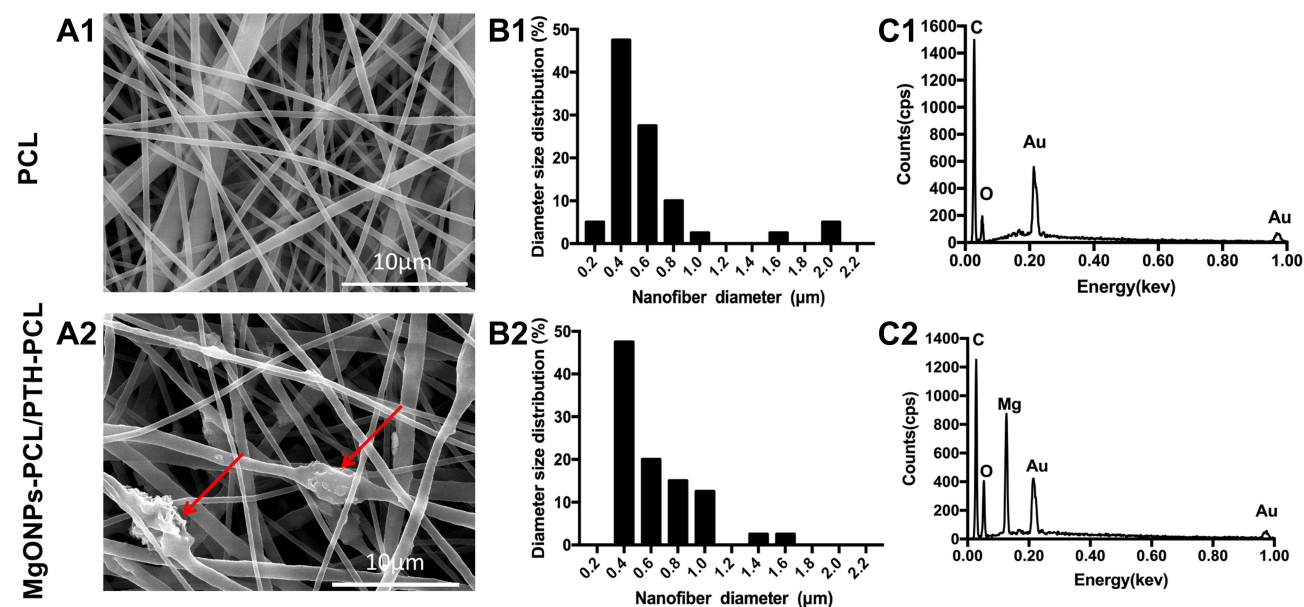


Figure 2 SEM image (A1, A2), fiber diameter distribution (B1, B2) and EDX spectra (C1, C2) of PCL and MgONPs-PCL/PTH-PCL membranes.

The pore sizes of pure PCL and the composite membrane were  $0.99 \pm 0.12\mu\text{m}$  and  $1.30 \pm 0.18\mu\text{m}$ , respectively, which could provide a sufficient barrier function since the pore sizes  $<10\mu\text{m}$  had been shown to efficiently prevent the invasion of surrounding connective tissue-derived fibroblasts and bacteria through the membrane.<sup>25,28</sup> Simultaneously, this also allowed the passage of essential chemicals and nutrients for bone regeneration.<sup>29</sup> The representative EDX spectra of the membranes are listed in Figure 2C1 and C2. Compared with pure PCL membrane, the composite membrane exhibited the presence of peak corresponded to Mg element and increased intensity of peak corresponded to O element (Figure 2C1), which indicated the incorporation of MgONPs in PCL (Figure C2). In addition, the quantitative EDX analysis of three randomly selected areas from the composite membranes are listed in Table 1. The data showed that the weight percentages of Mg in three different areas were 14.92%, 15.27% and 15.35%, respectively. In the meantime, the atomic percentages were 8.50%, 8.72% and 8.78%, respectively. The similar intensities of Mg peaks in the composite membrane revealed the homogeneous distribution of MgONPs.

### XRD and FTIR Test

The FTIR spectra of the membranes are exhibited in Figure 3A. The FTIR spectrum of pure PCL fiber (black curve) exhibited the stretching vibration at 2949, 2864, 1727, 1297 and  $1241\text{cm}^{-1}$ , which corresponded to asymmetric  $\text{CH}_2$  stretching, symmetric  $\text{CH}_2$  stretching, carbonyl stretching, C-O and C-C stretching in the crystalline phase, and asymmetric COC stretching, respectively.<sup>29,30</sup> These characteristic bands of PCL accordingly occurred at 2941, 2873, 1724, 1299 and  $1243\text{cm}^{-1}$  in the composite membrane. The spectrum of MgONPs exhibited the stretching vibration at  $870\text{cm}^{-1}$ , which corresponded to Mg-O bands.<sup>31</sup> The characteristic bands of PTH exhibited the stretching vibration at 1548 and  $1646\text{cm}^{-1}$ , which corresponded to amide bands.<sup>32</sup> The absorption peak of MgONPs (red curve) was not very prominent due to its much lower intensity than those of PCL. The XRD patterns of the pure PCL and MgONPs-PCL /PTH-PCL composite membranes are shown in Figure 3B. The pure PCL displayed two intense and sharp diffraction peaks at  $21.6^\circ$  and  $23.9^\circ$   $2\theta$ , which were attributed to the orthorhombic crystal structure of semi-crystalline PCL.<sup>33</sup> In addition to the characteristic peaks of PCL, the presence of MgONPs in the composite membrane resulted in the occurrence of two sharp diffraction peaks at  $43.0^\circ$  and  $62.1^\circ$ , which corresponded to its crystallographic planes.<sup>33</sup> The intensity of both the PCL peaks at  $21.6^\circ$  and  $23.9^\circ$  in the composite membrane decreased, which may be due to the incorporation of hydrophilic MgONPs and PTH lead to a decrease in degree of crystallinity of PCL.<sup>34,35</sup> All these results indicated that MgONPs and PTH were successfully incorporated into PCL fibers.

## Biological Evaluation

### PTH and MgONPs Release Profiles in-vitro

Figure 4A depicts the 29d accumulative release profiles of MgONPs from different membranes. The observed release profile of MgONPs from the MgONPs-PCL/PTH-PCL membrane comprised two distinct phases: the initial burst release on the first day (stage I) and a sustained release (stage II). At the initial stage, a concentration of approximately  $29.57 \pm 1.53\mu\text{g/mL}$  (14%) of MgONPs was released. This phenomenon may be attributed to the quick detachment of superficially distributed MgONPs on the nanofiber, resulting in a burst release.<sup>34</sup> Joyshree et al claim that MgONPs at a concentration of  $7.50\mu\text{g/mL}$  is sufficient to eliminate both gram-negative and gram-positive bacteria.<sup>36</sup> Furthermore, a previous study has also proposed that MgONPs at a concentration lower than  $500\mu\text{g/mL}$  are not cytotoxic.<sup>37</sup> This indicated that the abrupt release of MgONPs at stage 1 (within 24h) would contribute to eliminate the residual bacteria in periodontal

**Table 1** Quantitative EDX Analysis of Different Areas in MgONPs-PCL/PTH-PCL Composite Membrane (Wt%: Weight Percent, at%: Atom Percent)

Element	Area 1		Area 2		Area 3	
	Wt%	At%	Wt%	At%	Wt%	At%
C	62.11	71.62	61.56	71.17	61.02	70.67
O	22.97	19.88	23.17	20.11	23.63	20.55
Mg	14.92	8.50	15.27	8.72	15.35	8.78

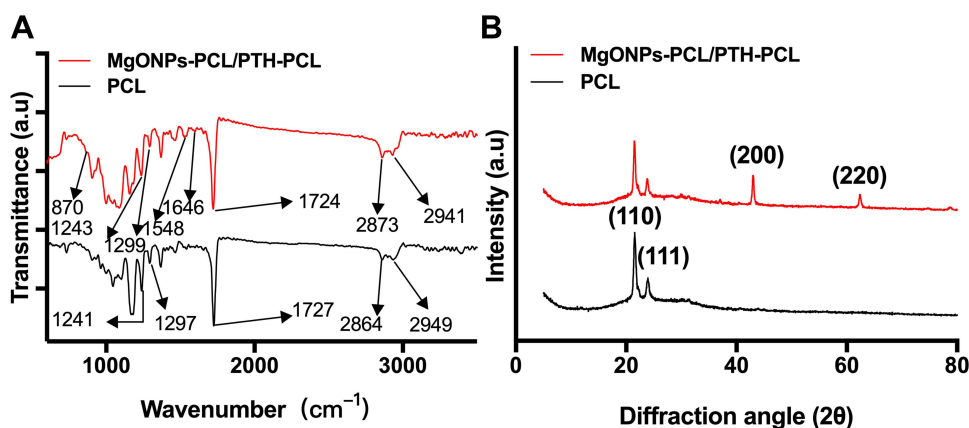


**Figure 3** (A) FTIR absorption spectroscopy and (B) XRD spectroscopy of PCL and MgONPs-PCL/PTH-PCL.

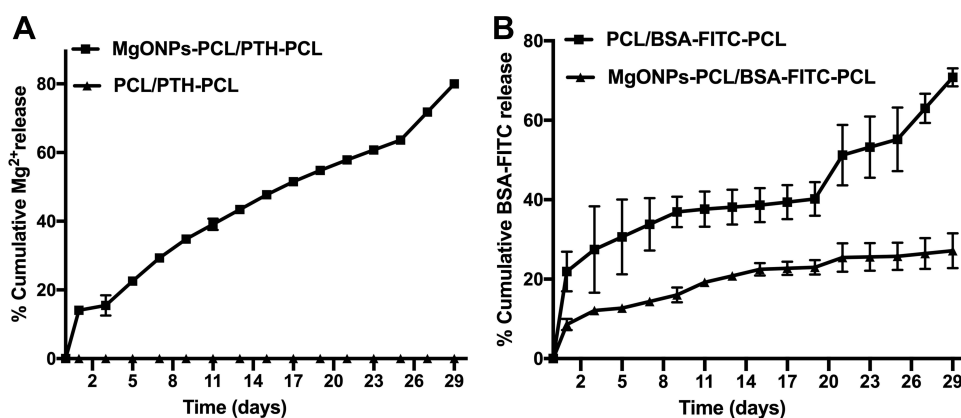


**Figure 4** The release profiles of (A)  $Mg^{2+}$  and (B) BSA-FITC from different membranes for 29 days.

tissues, thus preventing post-operative infections. Conversely, it was apparent that there was a sustained release of MgONPs for the remaining period at stage II with an average rate of 2.35% per day. This would aid in the inhibition of new bacterial invasion. According to the consensus of the 15th European Workshop on Periodontology on Bone Regeneration, exposure tolerance of GBR membrane is one of the basic requirements.<sup>38</sup> The early exposure of GBR membrane significantly compromises the regenerative outcomes of GBR.<sup>38</sup> The exposure tolerance is defined as

In case of exposure, the exposed membrane should be kept in situ and continue to function during the regenerative process, although in case of overt infections.<sup>38</sup>

In contrast to the limited exposure tolerance of commercially available GBR membranes,<sup>39</sup> the slow and sustained release of MgONPs and the low degradation rate of PCL (at pH=7, the PCL membrane just lose 11% of the initial weight after 50d degradation in PBS)<sup>40</sup> made MgONPs-PCL/PTH-PCL membrane possible to achieve exposure tolerance in the first month after implantation. Systemic administration of antibiotics and antiseptic mouthwash applied for a month post-operation were commonly used to prevent subsequent bacterial contamination for bone grafts through exposed wound.<sup>41</sup> The exposure tolerance of the membranes exhibited the potential to replace conventional methods, thereby avoiding the side effects such as drug resistance or disorders of normal oral flora.

To analyze the release profile of PTH, we utilized the BSA-FITC conjugate as a model protein.<sup>42</sup> The accumulative release profiles of BSA-FITC from different membranes in-vitro for 29d are listed in Figure 4B. BSA-FITC released from the membranes within 24h at rates of  $8.58 \pm 1.40\%$  (MgONPs-PCL/BSA-FITC-PCL) and  $21.95 \pm 5.02\%$  (PCL/BSA-FITC-PCL) per day of total amount of encapsulated BSA-FITC, respectively. The BSA-FITC in the core layer can

easily diffuse through the shells of nanofibers, resulting in the initial burst release.<sup>43</sup> Interestingly, the release profiles of BSA-FITC in different membranes showed a significant difference. The cumulative release percentage of BSA-FITC from the PCL/BSA-FITC-PCL membrane at day 29 was  $70.83 \pm 2.26\%$ , whereas only  $27.16 \pm 4.38\%$  of BSA-FITC was released from the MgONPs-PCL/BSA-FITC-PCL membrane. Ajay et al indicate that the degradation of PCL membrane will slowly release chain oligomers with acidic carboxyl groups, causing a slight acidification<sup>40</sup> in the surrounding milieu, which may reversely accelerate PCL degradation. It has been shown that the release and degradation of MgONPs will first cause a steep rise of pH to 8.1 and subsequent decrease at a slow rate, finally settling near 7.6.<sup>44</sup> Therefore, MgONPs-incorporation may regulate the release of PCL and thus BSA-FITC through neutralizing the pH of the surrounding milieu.<sup>40</sup> Thereby regenerated slow release of incorporated PTH was good to prevent bone resorption.<sup>45</sup> Additionally, the neutralized pH of the surrounding milieu prevented the negative effect on bone formation resulted from acid environment.<sup>46</sup> The release periods of PTH applied in local delivery system in previous studies were limited in 2w,<sup>32,47</sup> which was unable to cover the whole osteogenesis process (4w),<sup>48</sup> thereby may compromise the efficacy of GBR. Conversely, according to the result of BSA-FITC release profile of MgONPs-PCL/BSA-FITC-PCL membrane, there was approximately 70% BSA-FITC in storage at the end of the release study (29d), which satisfied the long-term osteogenesis process.

### In-vitro Antibacterial Efficacy

G. Rutger et al demonstrate that *T. forsythia* and *S. aureus* are associated with peri-implantitis.<sup>49</sup> Ter Boo et al declaim that gram-positive (such as *S. aureus* and *S. epidermidis*) and gram-negative (such as *Pseudomonas aeruginosa* and *E. coli*) bacteria are present in infected bone defects.<sup>50</sup> Hence, the antibacterial agent applied in the membrane should have a broad spectrum. For this purpose, we adopted two most widely used bacteria — *S. aureus* and *E. coli* to evaluate the antibacterial effect on gram-positive and gram-negative bacteria, respectively. Additionally, Gabrijela et al indicate that the bacteria adhesion on the membrane, which is considered a crucial initial stage for the formation of a biofilm, occurs in 4h.<sup>51</sup> Therefore, the elimination of residual bacteria in initial 24h was crucial for high efficacy of GBR. Based on this, we further evaluated the antibacterial efficacy of the membranes with or without MgONPs, which were co-cultured with bacteria for 24h using an MTT assay and listed it in Figure 5. Our data showed that MgONPs-PCL/PTH-PCL killed 95.04% *S. aureus* and 88.76% *E. coli* after an incubation for one day. In contrast, the non-MgONPs-containing membrane exhibited no significant antibacterial effect, instead, both types of bacteria proliferated in the presence of PCL/PTH-PCL membranes and culture medium. The dramatical reversal of antibacterial efficacy between the two membranes may attribute to the reactive oxygen species (ROS) of MgONPs. The free  $Mg^{2+}$  ions produced from the nanoparticle induced the uncontrolled ROS generation in bacteria, resulted in excessive oxidative stress, distorted cellular membrane, leakage of proteins, carbohydrates and lipids and eventually bacteria damage.<sup>52</sup> Hence, MgONPs-PCL/PTH-PCL was suggested a promising candidate for preventing post-operative infection.

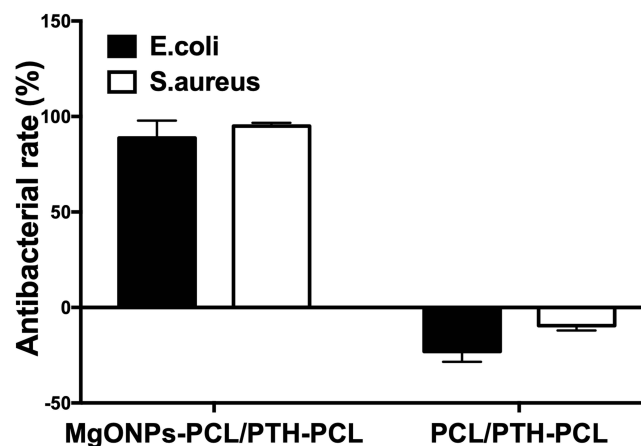


**Figure 5** Antibacterial effects of MgONPs-PCL/PTH-PCL and PCL/PTH-PCL against *S. aureus* and *E. coli*. Values are mean  $\pm$  SD from 3 independent experiments.

## The Effect of MgONPs-PCL/PTH-PCL Membrane on in-vitro Osteoblastic Activity

One desired property of the MgONPs-PCL/PTH-PCL membrane for GBR technique is to promote the proliferation and osteogenic differentiation of osteogenic cells. One potential contributor to this property may be the MgONPs-derived Mg, which has been shown to stimulate proliferation of osteoblasts.<sup>53</sup> On the other hand, overdosed MgONPs may be detrimental to cell viability through blocking DNA synthesis and cell cycle processes.<sup>54</sup> Therefore, a proper incorporation amount of MgONPs is highly important. In fact, the amount of incorporated MgONPs is mainly determined by the fabrication process and the antibacterial efficacy of MgONPs-PCL/PTH-PCL membrane. A relatively higher amount will result in high inhomogeneity with extensive bead-like structure on the nanofibers ([Supplement Data Figure S1](#)), while a relatively lower amount may not be sufficient to yield an adequate antibacterial efficacy ([Supplement Data Figure S2](#)). In our preliminary study, we screened the optimal dosage of MgONPs by assessing the morphology and antibacterial property, from which we determined the ratio of PCL: MgONPs at 1:0.3. With this dosage, the OD value of MC3T3-E1 pre-osteoblasts seeded on MgONPs-PCL/PCL was slightly higher than that seeded on pure PCL membrane ([Figure 6A](#)), which suggested no significant cytotoxicity of MgONPs at the current dosage. Albeit so, we did find that the presence of MgONPs was associated with significantly enhanced ALP activity — the early osteogenic differentiation markers ([Figure 6B](#)). One potential mechanism accounting for this promoting effect may be due to the MgONPs-derived Mg<sup>2+</sup> triggered upregulation of Akt phosphorylation and enhanced expression of osteogenic related genes.<sup>55</sup> Additionally, MgONPs-derived OH<sup>-</sup> stimulated the release of bone morphogenetic protein 2 and alkaline phosphatase.<sup>56</sup> However, MgONPs at the current dosage failed to significantly enhance extracellular matrix mineralization — the early osteogenic differentiation markers. To approach this problem, we adopted PTH to further enhance the pro-osteogenic property of the membrane. We showed that MgONPs-PCL/PTH20-PCL did significantly enhance cell proliferation ([Figure 6A](#)), ALP activity ([Figure 6B](#)) and extracellular matrix mineralization ([Figure 6C](#)) in comparison with both the pure PCL membrane and the MgONPs-PCL/PCL membrane. The potential mechanism accounting for this enhancing effect may be attributed to PTH that can stimulate the expression of osteoblast-specific transcription factors, thus promoting the

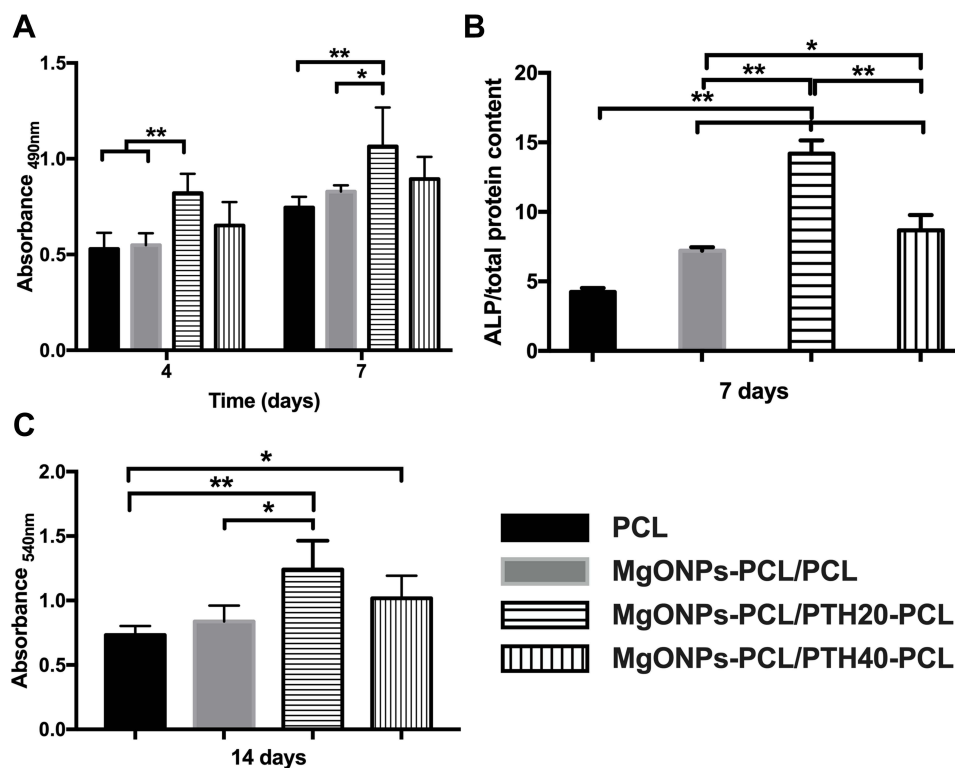


**Figure 6** The effects of PCL and MgONPs-PCL/PTHn-PCL membranes on (A) Proliferation of MC3T3-E1 cells, (B) Relative ALP activities of MC3T3-E1 cells and (C) Quantitatively detect of mineralization of MC3T3-E1 cells. Significant effect of treatment, \*\**p* < 0.01, \**p* < 0.05.

proliferation and differentiation of osteoblasts.<sup>57,58</sup> Mediated by PTH1R in early differentiated osteoblasts, PTH inactivates the proapoptotic factor Bad and the apoptosis-inducing factor CARP-1, while increases the expression of Bcl-2 and enhances DNA repair, thus reducing osteoblast apoptosis.<sup>59</sup>

### Micro-CT Observation

Calvarial bone defect in SD rats is one of the most widely used model to assess the osteogenic efficacy of biomaterials.<sup>60</sup> In previous literatures, 8-mm-in-diameter calvarial bone defects are regarded as critical-size bone defects with a maximum 10% healing within 13m.<sup>24,61</sup> In this study, we adopted the 8-mm-in-diameter calvarial bone defects to assess the osteogenic potential of MgONPs-PCL/PTH-PCL membranes in bacteria-contaminated defects.

4w post implantation, the implanted materials and surrounding tissues were retrieved, fixed and subjected to micro-CT analysis. In comparison with histological evaluation, Micro-CT is superior in both qualitatively and quantitatively evaluating the microstructure and mineral density of mineralized tissues.<sup>62,63</sup> As shown in the representative 3D reconstructed Micro-CT images of pure PCL group, the defects remained partially unfilled and largely unhealed with part of transplanted DBBM particles dislocated out of defects (Figure 7). In comparison, the addition of MgONPs resulted in significantly increased BV/TV and BV, as well as significant decreased Tb.Sp and DBBM dislocation, which might be due to the inhibition of bacterial activities of MgONPs. Interestingly, further significant improvement in BV/TV, Tb.N and Tb.Sp. was detected not in the group of MgONPs-PCL/PTH20-PCL but in the group of MgONPs-PCL/PTH40-PCL. This was inconsistent with our in-vitro cell result where MgONPs-PCL/PTH20-PCL but not MgONPs-PCL/PTH40-PCL resulted in significantly enhanced osteogenic differentiation of MC3T3-E1 cells. This was not unreasonable since the optimal dosage of bioactive agents in in-vivo model is often higher than that in in-vitro model.<sup>58,64</sup> Furthermore, the presence of bacteria in this in-vivo model might also partially deactivate PTH, which necessitate a higher concentration to exhibit a significant efficacy.

### Histological Assessment

We further adopted histological observations and histomorphometric analysis (Figure 8) to assess the newly formed bone tissue.<sup>65</sup> DBBM are deproteinized, decellularized and sintered bovine cancellous bone chips and its major component is hydroxyapatite.<sup>66</sup> Due to its excellent biocompatibility and osteoconductivity, DBBM is one of the most frequently used

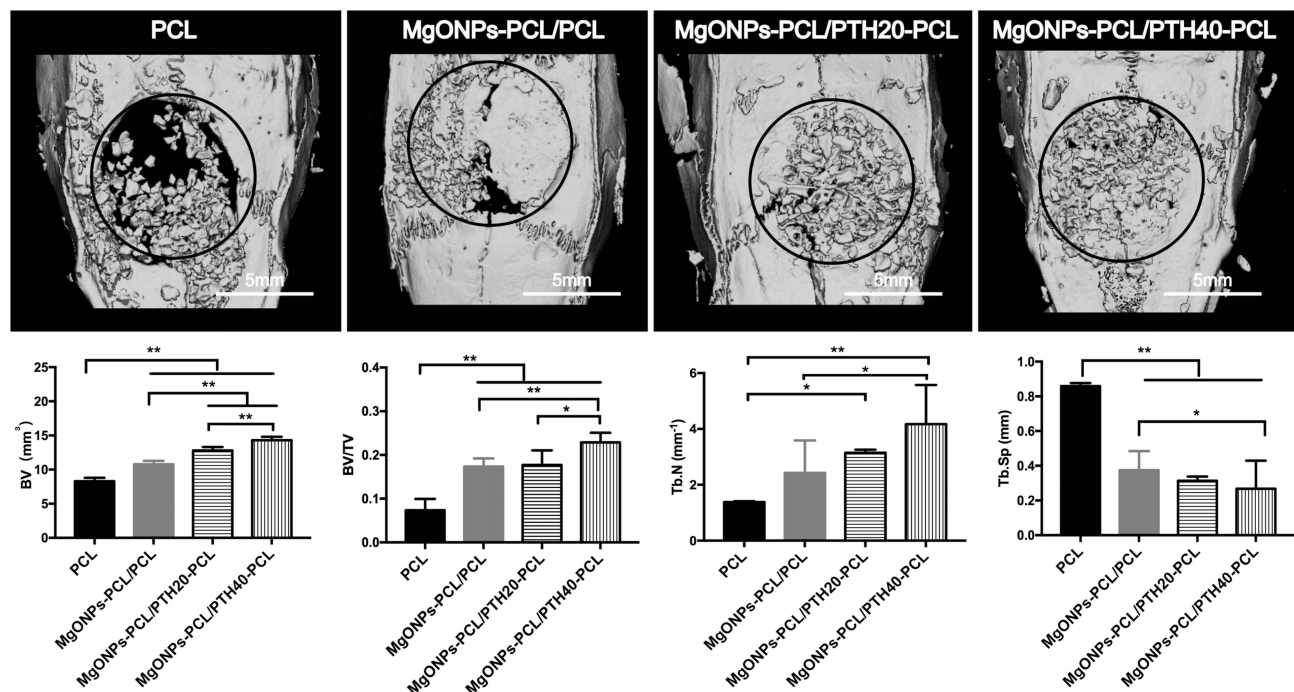


**Figure 7** Representative 3D micro-CT images of infective cranial bone defect rats with GBR process covering with different membranes from overall at week 4 post-operatively (The surgical regions are marked by black circle). Data of the selected regions are evaluated by micro-CT. Quantity analysis: Bone volume/Total volume (BV/TV), Bone volume (BV), Trabecular number (Tb. N) and Trabecular separation (Tb. Sp). Significant effect of treatment, \* $p < 0.05$ , \*\* $p < 0.01$ .

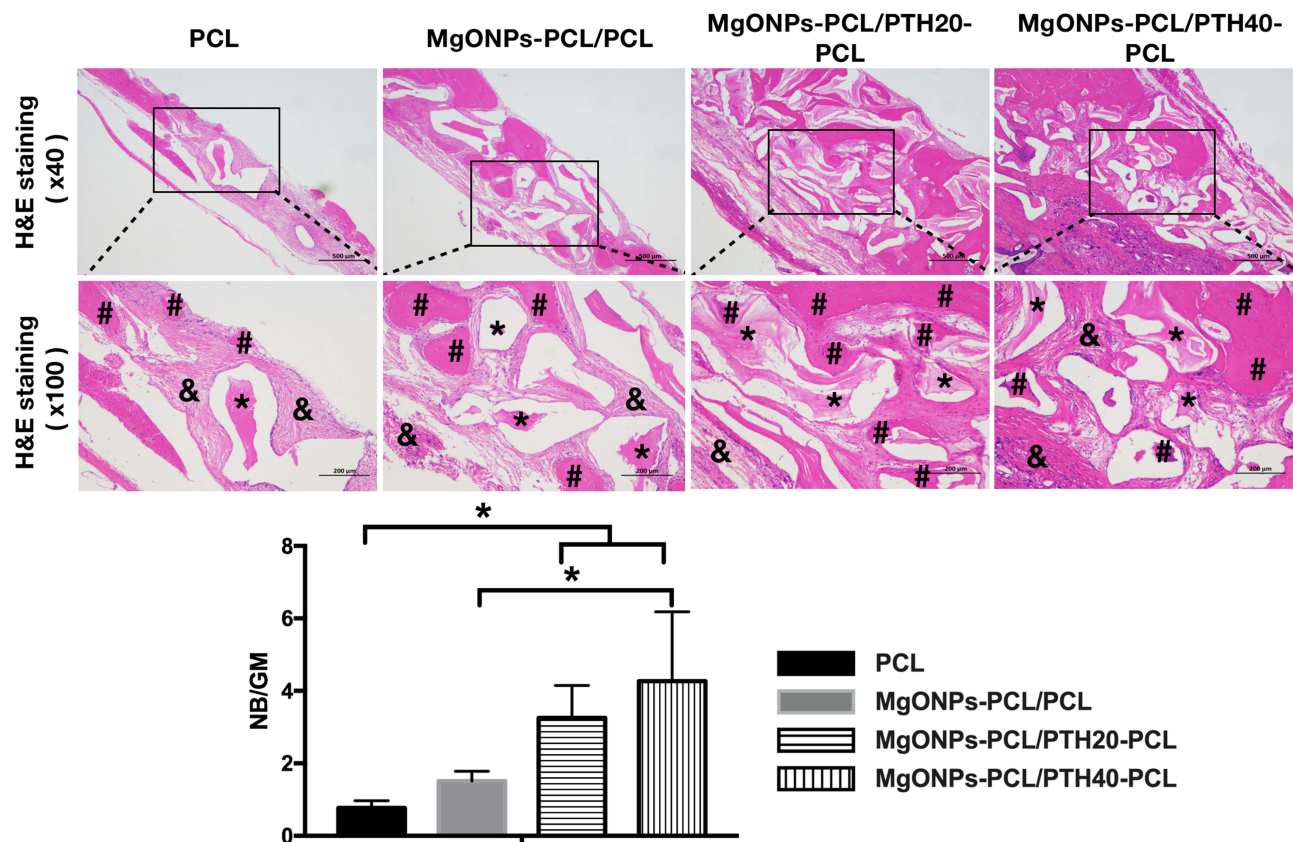


**Figure 8** H&E staining of infective cranial bone defect rats with GBR process covering with different membranes at week 4 post-operatively. DBBM granules (\*), new bone (#) and loose connective tissue (&) were marked in different groups H&E staining images. Quantity analysis of new bone as a percentage of graft material (new bone surface / entire graft materials surface; NB/GM). Significant effect of treatment, \* $p < 0.05$ .

materials in GBR technique.<sup>67</sup> After demineralization in the histological process, most of DBBM was dissolved, showing a morphology of vacuole. In some of the vacuoles, the undissolved DBBM formed an isolated island. In the group of PCL membrane, most of the vacuoles were surrounded by dense fibrous connective tissues. In the group of MgONPs-PCL/PCL, the fibrous newly formed tissue surrounding the vacuoles appeared to be less dense and there were some islands of new bone distributed within the connective tissues. There seemed no direct contact between new bone and vacuoles. In the two PTH-containing groups, more newly bone tissues were detected and formed direct contact with vacuoles. It seemed to be that the PTH-containing groups achieved a better bone-formation activity, thereby the presence of the osseous tissue suppressed the fibrous encapsulation of the DBBM. The quantity analysis of the new bone as a ratio of the graft material (new bone surface/entire graft materials surface; NB/GM) was calculated by imageJ software according to Young's study,<sup>68</sup> which was used to assess the osteogenesis efficacy. Consistent with the micro-CT finding, the histomorphometric analysis showed a slight promotion of NB/GM in MgONPs-PCL/ PCL while significantly promotion of that in the two PTH-containing groups compared with PCL. Furthermore, although there was no significant difference in two PTH-containing groups, the MgONPs-PCL/PTH40-PCL group showed a significantly promotion compared with MgONPs-PCL/ PCL group. It suggested that the osteogenesis of the MgONPs-PCL/PTH40-PCL membrane was mainly attributed to the incorporation of PTH. The existence of MgONPs was mainly acted as an antibacterial agent thus assisting the osteogenesis. Similar osteogenesis effects have also been observed by incorporating PTH in local drug delivery system, for instance, PTH-bound PEG hydrogel, PTH-fibrin matrix and PTH-incorporated CaP coating,<sup>32,47,69</sup> which indicated the local delivery system with an appropriate PTH dosage was a promising strategy for achieving osteogenesis.

## Conclusion

In this study, we have successfully synthesized a dual-functional nanofiber GBR membrane with antimicrobial and pro-osteogenic properties. The coaxial electrospinning procedure was used and successfully encapsulate a broad-spectrum antibacterial (MgONPs) agent in the shell layer and a pro-osteogenic drug (PTH) in the core layer of the nanofibers. The sustained release of MgONPs and PTH significantly promoted antibacterial property, which was shown in-vitro. This indicated that the membrane could effectively eliminate the residual bacteria in periodontal tissues. Furthermore, the results of release profiles and antibacterial assessments of the GBR membrane indicated its exposure tolerance for the first month after implantation. This would contribute to prevent GBR failure caused by early exposure. The significant improvement of osteogenesis in bacterial-contaminated models in-vivo, especially with the presence of high dosage PTH, proved to be a promising approach to satisfy the complicated and phased requirements of the GBR process in periodontitis or peri-implantitis patients with large-volume bone defects. In-depth mechanism research for the MgONPs and PTH interaction in micro-environment for the infection-defect bone area still needs further work.

## Acknowledgments

Authors acknowledge financial support provided by Wenzhou Municipal Science and Technology Project for Public Welfare (No. Y20190107 and No.2019Y0597).

## Author Contributions

All authors made a significant contribution to the work reported, whether that is in the conception, study design, execution, acquisition of data, analysis and interpretation, or in all these areas; took part in drafting, revising or critically reviewing the article; gave final approval of the version to be published; have agreed on the journal to which the article has been submitted; and agree to be accountable for all aspects of the work.

## Disclosure

The authors report no conflicts of interest in this work.

## References

1. Bottino MC, Thomas V, Schmidt G, et al. Recent advances in the development of GTR/GBR membranes for periodontal regeneration - A materials perspective. *Dent Mater*. 2012;28(7):703–721. doi:10.1016/j.dental.2012.04.022
2. Latimer JM, Maekawa S, Yao Y, Wu DT, Chen M, Giannobile W. Regenerative medicine technologies to treat dental, oral, and craniofacial defects. *Front Bioeng Biotechnol*. 2021;9:637. doi:10.3389/fbioe.2021.704048
3. Sheikh Z, Hamdan N, Ikeda Y, Grynepas M, Ganss B, Glogauer M. Natural graft tissues and synthetic biomaterials for periodontal and alveolar bone reconstructive applications: a review. *Biomater Res*. 2017;21(1):1–20. doi:10.1186/s40824-017-0095-5
4. Stahl A, Yang YP. Regenerative approaches for the treatment of large bone defects. *Tissue Eng Part B Rev*. 2021;27(6):539–547. doi:10.1089/ten.teb.2020.0281
5. Shoba E, Lakra R, Kiran MS, Korrapati PS. 3 D nano bilayered spatially and functionally graded scaffold impregnated bromelain conjugated magnesium doped hydroxyapatite nanoparticle for periodontal regeneration. *J Mech Behav Biomed Mater*. 2020;109:103822. doi:10.1016/j.jmbbm.2020.103822
6. Zhang R, Yang J, Wu J, et al. Berberine promotes osteogenic differentiation of mesenchymal stem cells with therapeutic potential in periodontal regeneration. *Eur J Pharmacol*. 2019;851:144–150. doi:10.1016/j.ejphar.2019.02.026
7. Calamak S, Shahbazi R, Eroglu I, Gultekinoglu M, Ulubayram K. An overview of nanofiber-based antibacterial drug design. *Expert Opin Drug Discov*. 2017;12(4):391–406. doi:10.1080/17460441.2017.1290603
8. Isola G, Polizzi A, Santonocito S, Dalessandri D, Migliorati M, Indelicato F. New frontiers on adjuvants drug strategies and treatments in periodontitis. *Sci Pharm*. 2021;89(4):46. doi:10.3390/scipharm89040046
9. Makvandi P, Josic U, Delfi M, et al. Drug delivery (nano)platforms for oral and dental applications: tissue regeneration, infection control, and cancer management. *Adv Sci*. 2021;8(8):2004014. doi:10.1002/adv.202004014
10. Blecher K, Nasir A, Friedman A. The growing role of nanotechnology in combating infectious disease. *Virulence*. 2011;2(5):395–401. doi:10.4161/viru.2.5.17035
11. Sanders CC, Sanders WE, Harrowe DJ. Bacterial interference: effects of oral antibiotics on the normal throat flora and its ability to interfere with group A streptococci. *Infect Immun*. 1976;13(3):808–812. doi:10.1128/iai.13.3.808-812.1976
12. Hornak J. Synthesis, properties and selected technical applications of magnesium oxide nanoparticles: a review. *Int J Mol Sci*. 2021;22(23):12752. doi:10.3390/ijms222312752
13. Eivazzadeh-Keihan R, Bahojb Noruzi E, Khanmohammadi chenab K, et al. Metal-based nanoparticles for bone tissue engineering. *J Tissue Eng Regen Med*. 2020;14(12):1687–1714. doi:10.1002/term.3131

14. Hayat S, Muzammil S, Rasool MH, et al. In vitro antibiofilm and anti-adhesion effects of magnesium oxide nanoparticles against antibiotic resistant bacteria. *Microbiol Immunol*. 2018;62(4):211–220. doi:10.1111/1348-0421.12580
15. Meenashisundaram GK, Wang N, Maskomani S, et al. Fabrication of Ti + Mg composites by three-dimensional printing of porous Ti and subsequent pressureless infiltration of biodegradable Mg. *Mater Sci Eng C*. 2020;108:110478. doi:10.1016/j.msec.2019.110478
16. Safari B, Davaran S, Aghanejad A. Osteogenic potential of the growth factors and bioactive molecules in bone regeneration. *Int J Biol Macromol*. 2021;175:544–557. doi:10.1016/j.ijbiomac.2021.02.052
17. Cannata-andia JB, Carrillo-lópez N, Messina OD, Hamdy NAT, Panizo S, Ferrari SL. Pathophysiology of vascular calcification and bone loss: linked disorders of ageing? *Nutrients*. 2021;13(11):3835. doi:10.3390/nu13113835
18. Dang M, Saunders L, Niu X, Fan Y, Ma PX. Biomimetic delivery of signals for bone tissue engineering. *Bone Res*. 2018;6(1):1–12. doi:10.1038/s41413-018-0025-8
19. Feng P, Zhao R, Yang L, et al. Hydrothermal synthesis of hydroxyapatite nanorods and their use in PCL bone scaffold. *Ceram Int*. 2022;48(22):33682–33692. doi:10.1016/j.ceramint.2022.07.314
20. Feng P, Wang K, Shuai Y, Peng S, Hu Y, Shuai C. Hydroxyapatite nanoparticles in situ grown on carbon nanotube as a reinforcement for poly( $\epsilon$ -caprolactone) bone scaffold. *Mater Today Adv*. 2022;15:100272. doi:10.1016/j.mtadv.2022.100272
21. Wu G, Hunziker EB, Zheng Y, Wismeijer D, Liu Y. Functionalization of deproteinized bovine bone with a coating-incorporated depot of BMP-2 renders the material efficiently osteoinductive and suppresses foreign-body reactivity. *Bone*. 2011;49(6):1323–1330. doi:10.1016/j.bone.2011.09.046
22. Dong Y, Ye H, Liu Y, et al. pH dependent silver nanoparticles releasing titanium implant: a novel therapeutic approach to control peri-implant infection. *Colloids Surf B Biointerfaces*. 2017;158:127–136. doi:10.1016/j.colsurfb.2017.06.034
23. Wen Y, Zhou W, Zhu X, et al. An investigation of circadian rhythm in *Escherichia coli*. *Biol Rhythm Res*. 2015;46(5):753–762. doi:10.1080/09291016.2015.1052650
24. Schmitz JP, Hollinger JO. The critical size defect as an experimental model for craniomandibulofacial nonunions. *Clin Orthop Relat Res*. 1986;205:299–308. doi:10.1097/00003086-198604000-00036
25. Liu X, He X, Jin D, et al. A biodegradable multifunctional nanofibrous membrane for periodontal tissue regeneration. *Acta Biomater*. 2020;108:207–222. doi:10.1016/j.actbio.2020.03.044
26. Yang F, Both SK, Yang X, Walboomers XF, Jansen JA. Development of an electrospun nano-apatite/PCL composite membrane for GTR/GBR application. *Acta Biomater*. 2009;5(9):3295–3304. doi:10.1016/j.actbio.2009.05.023
27. Chen M, Patra PK, Warner SB, Bhowmick S. Role of fiber diameter in adhesion and proliferation of NIH 3T3 fibroblast on electrospun polycaprolactone scaffolds. *Tissue Eng*. 2007;13(3):579–587. doi:10.1089/ten.2006.0205
28. Qasim SB, Delaine-Smith RM, Fey T, Rawlinson A, Rehman IU. Freeze gelled porous membranes for periodontal tissue regeneration. *Acta Biomater*. 2015;23:317–328. doi:10.1016/j.actbio.2015.05.001
29. Mallakpour S, Nouruzi N. Effect of modified ZnO nanoparticles with biosafe molecule on the morphology and physiochemical properties of novel polycaprolactone nanocomposites. *Polyme*. 2016;89:94–101. doi:10.1016/j.polymer.2016.02.038
30. Polini A, Pisignano D, Parodi M, Quarto R, Scaglione S. Osteoinduction of human mesenchymal stem cells by bioactive composite scaffolds without supplemental osteogenic growth factors. *PLoS One*. 2011;6(10):e26211. doi:10.1371/journal.pone.0026211
31. Peia LZ, Yinb LZ, Wang JF, Chena J, Fana CG, Zhang QF. Low temperature synthesis of magnesium oxide and spinel powders by a sol-gel process. *Mater Res*. 2010;13(3):339–343. doi:10.1590/s1516-14392010000300010
32. Yu X, Wei M. Preparation and evaluation of parathyroid hormone incorporated CaP coating via a biomimetic method. *J Biomed Mater Res B Appl Biomater*. 2011;97 B(2):345–354. doi:10.1002/jbm.b.31820
33. Lee KH, Kim HY, Khil MS, Ra YM, Lee DR. Characterization of nano-structured poly( $\epsilon$ -caprolactone) nonwoven mats via electrospinning. *Polyme*. 2003;44(4):1287–1294. doi:10.1016/S0032-3861(02)
34. Adhikari U, An X, Rijal N, et al. Embedding magnesium metallic particles in polycaprolactone nanofiber mesh improves applicability for biomedical applications. *Acta Biomater*. 2019;98:215–234. doi:10.1016/j.actbio.2019.04.061
35. Coelho CC, Araújo R, Quadros PA, Sousa SR, Monteiro FJ. Antibacterial bone substitute of hydroxyapatite and magnesium oxide to prevent dental and orthopaedic infections. *Mater Sci Eng C*. 2019;97:529–538. doi:10.1016/j.msec.2018.12.059
36. Maji J, Pandey S, Basu S. Synthesis and evaluation of antibacterial properties of magnesium oxide nanoparticles. *Bull Mater Sci*. 2020;43(1):1–10. doi:10.1007/s12034-019-1963-5
37. Wetteland CL, Nguyen NYT, Liu H. Concentration-dependent behaviors of bone marrow derived mesenchymal stem cells and infectious bacteria toward magnesium oxide nanoparticles. *Acta Biomater*. 2016;35:341–356. doi:10.1016/j.actbio.2016.02.032
38. Sanz M, Dahlin C, Apatzidou D, et al. Biomaterials and regenerative technologies used in bone regeneration in the craniomaxillofacial region: consensus report of group 2 of the 15th European Workshop on periodontology on bone regeneration. *J Clin Periodontol*. 2019;46(S21):82–91. doi:10.1111/jcpe.13123
39. Chen K, Zhou G, Li Q, et al. In vitro degradation, biocompatibility and antibacterial properties of pure zinc: assessing the potential of Zn as a guided bone regeneration membrane. *J Mater Chem B*. 2021;9(25):5114–5127. doi:10.1039/d1tb00596k
40. Scaffaro R, Lopresti F, Botta L. Preparation, characterization and hydrolytic degradation of PLA/PCL co-mingled nanofibrous mats prepared via dual-jet electrospinning. *Eur Polym J*. 2017;96:266–277. doi:10.1016/j.eurpolymj.2017.09.016
41. Ocaña RP, Rabelo GD, Sassi LM, Rodrigues VP, Alves FA. Implant osseointegration in irradiated bone: an experimental study. *J Periodontol Res*. 2017;52(3):505–511. doi:10.1111/jre.12416
42. Coq N, van Bommel T, Hikmet RA, Stapert HR, Dittmer WU. Self-supporting hydrogel stamps for the microcontact printing of proteins. *Langmuir*. 2007;23(9):5154–5160. doi:10.1021/la0700321
43. Choi JS, Yoo HS. Nano-inspired fibrous matrix with bi-phasic release of proteins. *J Nanosci Nanotechnol*. 2010;10(5):3038–3045. doi:10.1166/jnn.2010.2164
44. Suryavanshi A, Khanna K, Sindhu KR, Bellare J, Srivastava R. Magnesium oxide nanoparticle-loaded polycaprolactone composite electrospun fiber scaffolds for bone-soft tissue engineering applications: in-vitro and in-vivo evaluation. *Biomedical Materials*. 2017;12(5):055011. doi:10.1088/1748-605X/aa792b

45. Jilka RL, O'Brien CA, Bartell SM, Weinstein RS, Manolagas SC. Continuous elevation of PTH increases the number of osteoblasts via both osteoclast-dependent and -independent mechanisms. *J Bone Miner Res.* 2010;25(11):2427–2437. doi:10.1002/jbmr.145
46. Liu J, Kerns DG. Mechanisms of guided bone regeneration: a review. *Open Dent J.* 2014;8(1):56. doi:10.2174/1874210601408010056
47. Jung RE, Cochran DL, Domken O, et al. The effect of matrix bound parathyroid hormone on bone regeneration. *Clin Oral Implants Res.* 2007;18(3):319–325. doi:10.1111/j.1600-0501.2007.01342.x
48. Gomes PS, Fernandes MH. Rodent models in bone-related research: the relevance of calvarial defects in the assessment of bone regeneration strategies. *Lab Anim.* 2011;45(1):14–24. doi:10.1258/la.2010.010085
49. Persson GR, Renvert S. Cluster of bacteria associated with peri-implantitis. *Clin Implant Dent Relat Res.* 2014;2014:783–793. doi:10.1111/cid.12052
50. ter Boo GJA, Grijpma DW, Moriarty TF, Richards RG, Eglin D. Antimicrobial delivery systems for local infection prophylaxis in orthopedic- and trauma surgery. *Biomaterials.* 2015;52(1):113–125. doi:10.1016/j.biomaterials.2015.02.020
51. Begić G, Petković Didović M, Lučić Blagojević S, et al. Adhesion of oral bacteria to commercial d-PTFE membranes: polymer microstructure makes a difference. *Int J Mol Sci.* 2022;23(6):2983. doi:10.3390/ijms23062983
52. Bhattacharya P, Dey A, Neogi S. An insight into the mechanism of antibacterial activity by magnesium oxide nanoparticles. *J Mater Chem B.* 2021;9(26):5329–5339. doi:10.1039/d1tb00875g
53. Pang KM, Lee JW, Lee JY, et al. Clinical outcomes of magnesium-incorporated oxidised implants: a randomised double-blind clinical trial. *Clin Oral Implants Res.* 2014;25(5):616–621. doi:10.1111/clr.12091
54. Mahmoud A, Ö E, Merve A, Özhan G. In vitro toxicological assessment of magnesium oxide nanoparticle exposure in several mammalian cell types. *Int J Toxicol.* 2016;429–437. doi:10.1177/1091581816648624
55. Wang J, Ma XY, Feng YF, et al. Magnesium ions promote the biological behaviour of rat calvarial osteoblasts by activating the PI3K/Akt signalling pathway. *Biol Trace Elem Res.* 2017;179(2):284–293. doi:10.1007/s12011-017-0948-8
56. Radha R, Sreekanth D. Insight of magnesium alloys and composites for orthopedic implant applications – a review. *J Magnes Alloys.* 2017;5(3):286–312. doi:10.1016/j.jma.2017.08.003
57. Balani DH, Ono N, Kronenberg HM. Parathyroid hormone regulates fates of murine osteoblast precursors in vivo. *J Clin Invest.* 2017;127(9):3327–3338. doi:10.1172/JCI91699
58. Jang MG, Lee JY, Yang JY, et al. Intermittent PTH treatment can delay the transformation of mature osteoblasts into lining cells on the periosteal surfaces. *J Bone Miner Metab.* 2016;34(5):532–539. doi:10.1007/s00774-015-0707-x
59. Silva BC, Bilezikian JP. Parathyroid hormone: anabolic and catabolic actions on the skeleton. *Curr Opin Pharmacol.* 2015;22:41–50. doi:10.1016/j.coph.2015.03.005
60. An YH, Friedman RJ. Animal models of bone defect repair. *Anim Mod Orthopaedic Res.* 2020;241–260. doi:10.1201/9780429173479-16
61. Takagi K, Urist MR. The reaction of the dura to bone morphogenetic protein (BMP) in repair of skull defects. *Ann Surg.* 1982;196(1):100. doi:10.1097/0000658-198207000-00020
62. Jiang Y, Zhao J, Liao EY, Dai RC, Wu XP, Genant HK. Application of micro-ct assessment of 3-d bone microstructure in preclinical and clinical studies. *J Bone Miner Metab.* 2005;23(SUPPL.1):122–131. doi:10.1007/BF03026336
63. Thomsen JS, Laib A, Koller B, Prohaska S, Mosekilde L, Gowin W. Stereological measures of trabecular bone structure: comparison of 3D micro computed tomography with 2D histological sections in human proximal tibial bone biopsies. *J Microsc.* 2005;218(2):171–179. doi:10.1111/j.1365-2818.2005.01469.x
64. Wang J, Li J, Yang L, Zhou Y, Wang Y. Dose-dependence of PTH-related peptide-1 on the osteogenic induction of MC3T3-E1 cells in vitro. *Medicine.* 2017;96(17):e6637. doi:10.1097/MD.0000000000006637
65. D'Lima JP, Paul J, Palathingal P, Varma BRR, Bhat M, Mohanty M. Histological and histometrical evaluation of two synthetic hydroxyapatite based biomaterials in the experimental periodontal defects in dogs. *J Clin Diagn Res.* 2014;8(9):ZC52. doi:10.7860/JCDR/2014/9892.4860
66. Retzepi M, Donos N. Guided bone regeneration: biological principle and therapeutic applications. *Clin Oral Implants Res.* 2010;21(6):567–576. doi:10.1111/j.1600-0501.2010.01922.x
67. Verket A, Lyngstadaas SP, Tiainen H, Rønold HJ, Wohlfahrt JC. Impact of particulate deproteinized bovine bone mineral and porous titanium granules on early stability and osseointegration of dental implants in narrow marginal circumferential bone defects. *Int J Oral Maxillofac Surg.* 2018;47(8):1086–1094. doi:10.1016/j.ijom.2018.02.007
68. Kim YK, Kim SG, Lim SC, Lee HJ, Yun PY. A clinical study on bone formation using a demineralized bone matrix and resorbable membrane. *Oral Surg Oral Med Oral Path Oral Radiol Oral Endodontology.* 2010;109(6):e6–e11. doi:10.1016/j.tripleo.2010.01.012
69. Arrighi I, Mark S, Alvisi M, von Rechenberg B, Hubbell JA, Schense JC. Bone healing induced by local delivery of an engineered parathyroid hormone produg. *Biomaterials.* 2009;30(9):1763–1771. doi:10.1016/j.biomaterials.2008.12.023